

Surface Brillouin scattering study of the surface excitations in amorphous silicon layers produced by ion bombardment

X. Zhang, J. D. Comins, A. G. Every, P. R. Stoddart, and W. Pang

Condensed Matter Physics Research Unit and Department of Physics, University of the Witwatersrand, Johannesburg, Wits 2050, South Africa

T. E. Derry

Schonland Research Centre for Nuclear Sciences and Department of Physics, University of the Witwatersrand, Johannesburg, Wits 2050, South Africa

(Received 3 June 1998)

Thin amorphous silicon layers on crystalline silicon substrates have been produced by argon-ion bombardment of (001) silicon surfaces. Thermally induced surface excitations characteristic of this example of a soft-on-hard system have been investigated by surface Brillouin scattering (SBS) as a function of scattering-angle and amorphous-layer thickness. At large scattering angles or for sufficiently large layer thickness, a second peak is present in the SBS spectrum near the low-energy threshold for the continuum of bulk excitations of the system. The measured spectra are analyzed on the basis of surface elastodynamic Green's functions, which successfully simulate their detailed appearance and identify the second peak as either a Sezawa wave (true surface wave) or a pseudo-Sezawa wave (attenuated surface wave) depending on the scattering parameters. The attributes of the pseudo-Sezawa wave are described; these include its asymmetrical line shape and variation in intensity with $k_{\parallel}d$ (the product of the surface excitation wave vector and the layer thickness), and its emergence as the Sezawa wave from the low-energy side of the Lamb shoulder at a critical value of $k_{\parallel}d$. Furthermore, the behavior of a pronounced minimum in the Lamb shoulder near the longitudinal wave threshold observed in the experiments is reported and is found to be in good agreement with the calculated spectra. The elastic constants of the amorphous silicon layer are determined from the velocity dispersion of the Rayleigh surface acoustic wave and the minimum in the Lamb shoulder. [S0163-1829(98)04039-9]

I. INTRODUCTION

Surface Brillouin scattering (SBS) is proving to be of great value in the study of the acoustic excitations and elastic properties of thin-supported layers and multilayers.¹⁻⁶ Thermally excited phonons in the GHz frequency range are responsible for the light scattering, and for opaque materials, the scattering is mediated principally by the surface ripple mechanism. The combination of substrate and overlayer determines the types of surface excitations and whether they can be observed by SBS. Depending on the physical and experimental parameters, these excitations may include Rayleigh surface acoustic waves (Rayleigh SAW's), pseudo-SAW's, Sezawa and pseudo-Sezawa waves, the continuum of bulk waves comprising the Lamb shoulder, and, in certain cases Stoneley interfacial waves. The inelastically scattered light tends to be low in intensity and only fractionally frequency shifted as compared with the elastically scattered light, but the combination of modern high-contrast tandem Fabry-Pérot interferometry and sensitive detectors allows the spectrum to be measured. Theoretical modeling on the basis of surface Green's functions or otherwise, and fitting to measured spectra allows critical material parameters of the system to be determined. Recently, we have studied a variety of surface acoustic excitations in the technologically important combination TiN on high-speed steel in this manner.⁸ As a result of its relatively high elastic moduli, TiN has a stiffening effect on the surface-wave velocity; with increasing layer thickness this velocity merges into the bulk continuum and

the associated mode becomes a pseudo-SAW.

In the present work, we examine the converse situation of a layer with relatively lower elastic constants as compared with the substrate. This leads to a reduction of the Rayleigh SAW velocity and the formation of higher-order modes known as Sezawa and pseudo-Sezawa waves, which are the main concern of this paper. True Sezawa waves are surface waves in which the particle displacements are mainly localized in the layer, falling off exponentially in the substrate; when the sagittal plane is a symmetry plane of the material, they are polarized in this plane. It is known from previous investigations that waves of this type can exist when the transverse bulk-wave velocity in the layer V_t^l is smaller than that in the substrate V_t^s and only for a restricted range of $k_{\parallel}d$ (the product of the surface excitation wave vector and the layer thickness).^{1,5,7} However, Sezawa-like peaks corresponding to attenuated excitations are still observed experimentally when this critical condition is not satisfied.^{3,4,9} Mutti *et al.*¹ used the term pseudo-Sezawa waves for such resonances that lie within the Lamb shoulder. Our studies examine these interesting excitations experimentally and theoretically for the values of $k_{\parallel}d$ in the region of the critical condition determining their emergence as true surface excitations. We describe the buildup of their asymmetrical line shape near the edge of the Lamb shoulder as the critical condition is approached, and how this resonance subsequently subsides as the Sezawa wave separates from the bulk-wave continuum. Moreover, we show that the edge of

the Lamb shoulder corresponds to the transonic state, which for anisotropic solids does not in general coincide with V_T^s .

A silicon crystal with an amorphous surface layer formed by ion bombardment is an advantageous system in which to study Sezawa-type excitations, since the elastic constants of amorphous silicon are appreciably smaller than those of crystalline silicon,^{10–12} while the layer thickness can be easily changed by varying the ion energy. We shall justify the uniformity of the amorphous layers in some detail in a later section of the paper.

We have performed a series of SBS measurements at different scattering angles, and hence different values of the projected wave vector k_{\parallel} along the [100] direction referred to the (001) crystalline silicon substrate, on a series of amorphous silicon layers of different thickness d . In addition to the Rayleigh SAW, a peak was observed near the Lamb shoulder, but only under conditions of large scattering angle and for large layer thickness. A comparison with theory reveals that these features are due to Sezawa or pseudo-Sezawa wave peaks, depending on the experimental parameters.

We have also studied a minimum that occurs in the Lamb shoulder near the longitudinal threshold, and how it changes with scattering angle. In this paper, we show that the experimental measurements of these various excitations and their relatively complex behavior are well described when the surface dynamics are modeled using Green's functions and optimized fitting is able to yield the elastic constants of the amorphous layer.

II. SAMPLE PREPARATION AND EXPERIMENTAL TECHNIQUE

Suitable samples of approximate dimensions 16 mm^2 were cut from a large n -type crystalline silicon wafer having a chemically polished (001) surface. The phosphorus impurity concentration was approximately 10^{16} cm^{-3} , sufficiently low to ensure negligible effects on the elastic constants of silicon.¹³ The samples were bombarded at room temperature by argon ions of energy ranging from 30–150 keV. A region of 3.8 mm in diameter was bombarded in each case with the ion beam tilted about 7° away from the [001] crystallographic direction to reduce ion channeling.¹⁴ All samples were bombarded with the same relatively high fluence of $1 \times 10^{17} \text{ ions/cm}^2$; in each case the total ion current was maintained at $30 \mu\text{A}$. The sample designation and ion energies are A (150 keV), B (120 keV), C (90 keV), D (60 keV), and E (30 keV).

The above bombardment conditions were carefully chosen to provide an excellent approximation to the theoretical model investigated, namely, that of an elastically uniform isotropic amorphous silicon layer on the (001) crystalline silicon surface. This claim is based on the results of previous studies in which crystalline silicon is shown to become completely amorphous from argon or krypton-ion bombardment for fluences greater than $5 \times 10^{15} \text{ ions/cm}^2$.^{10,15,16} The fluence of $1 \times 10^{17} \text{ ions/cm}^2$ ensures that the fully amorphized state is obtained in the entire region of the vacancy distribution, as determined by TRIM 92 calculations.¹⁴ Figure 1 shows the TRIM simulations of the vacancy distributions for silicon bombarded by argon ions. These distributions are however, quiet unphysical for our case: the average number

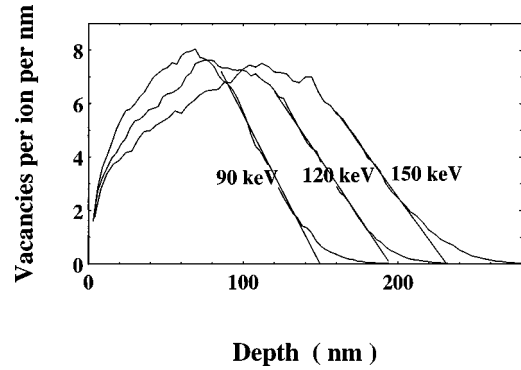


FIG. 1. TRIM 92 simulations of the vacancy distributions in silicon bombarded using different argon ion energies of 90, 120, and 150 keV, respectively, corresponding to samples C, B, and A. The lines are straight-line extrapolations of the deep-edge tail of the distributions.

of vacancies per ion is about 1200, giving a peak vacancy concentration for the fluence used, of about 10^{25} cm^{-3} or 100 times the atomic density of silicon. In other words, each atom at the peak of the distribution has been displaced about 100 times. The entire region of the vacancy distribution must therefore be uniformly amorphous up to the point where the deep-edge tail has fallen to about 0.01 of the peak height. We use simple straight-line extrapolations of the deep-edge tail to determine the thickness of the completely amorphous region as shown. There is still a region where the fully amorphized state is not achieved, but it is only a small fraction of the layer thickness. The amorphous nature of the layer was also confirmed by additional tests to be described in Sec. IV below.

SBS spectra were gathered for samples A–E using the 514.5 nm line from an argon-ion laser operating in a single axial mode. In illuminating each sample, the laser beam was focused onto the sample by a lens of aperture $f/2.3$ in a back-scattering arrangement as shown in Fig. 2. The wave vector \mathbf{k}_i of the incident light makes an angle θ with the surface normal, and the light back scattered into a small cone around $-\mathbf{k}_i$ is collected by the same lens. Momentum and energy conservation demands that the wave vector k_{\parallel} and velocity V of a surface acoustic wave must satisfy the following equations:

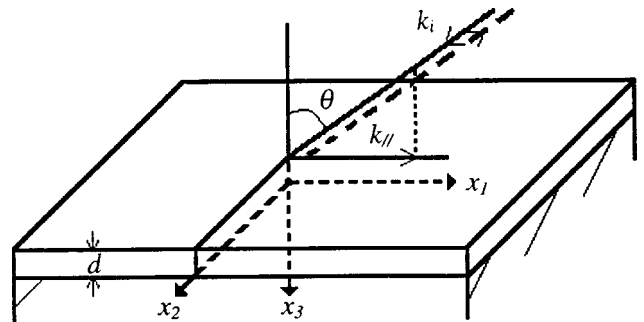


FIG. 2. Sample geometry and scattering configuration. The x_1 and x_2 axes are parallel to the surface of the sample; the x_1 axis is along the [100] direction of crystalline silicon, the x_3 axis is normal to the surface of the sample and along the [001] direction. The origin of the x_3 axis is taken at the interface.

$$k_{\parallel} = 2k_i \sin \theta,$$

$$V = \omega/k_{\parallel},$$

where ω is the change in angular frequency of the scattered light. The scattered spectrum was analyzed by a Sandercock (3 + 3) pass tandem Fabry-Pérot interferometer. The detector was a Hamamatsu R464S cooled photomultiplier with a dark count of less than one per second or a SPCM-PQ detector, based on a special high-quantum efficiency silicon avalanche photodiode with a dark count of one per second, when low-intensity excitations were monitored. An acousto-optic modulator was used to protect the detectors from excessive light from the intense elastic peak.

Procedures to minimize errors resulting from the collection aperture are treated in recent papers.^{1,17} In order to obtain the same measurement accuracy at different scattering angles, slits of the appropriate size were used to limit the collection aperture of the scattered light entering the interferometer.

III. THEORY OF BRILLOUIN SCATTERING FROM THE SURFACE OF A SUPPORTED LAYER

We consider light scattering from an opaque layer perfectly bonded to its substrate. The coordinate system we adopt is shown in Fig. 2 with $-x_3$ as the outward normal to the solid surface and with the origin at the interface between the layer and the substrate. The substrate occupies the half space $x_3 > 0$ and the layer, which is of thickness d , occupies the region $-d < x_3 < 0$.

As discussed in the literature,¹⁸⁻²¹ surface-acoustic vibrations result in the surface of a solid being dynamically corrugated to incident light. This surface ripple mechanism of light scattering dominates elasto-optic scattering for nearly opaque solids and provides a satisfactory description of the light scattering by surface excitations in the present work. The scattering cross section for change in angular frequency ω and surface-wave wave vector k_{\parallel} of the light is proportional to the power spectrum of the normal displacements of the surface with that wave vector and at that frequency. In turn, for sufficiently high temperatures $T \gg \hbar \omega/k_B$, where k_B is Boltzmann's constant, the scattering efficiency or cross section is given by¹⁸⁻²¹

$$I(\omega) = D \frac{T}{\omega} \text{Im}\{G_{33}(k_{\parallel}, x_3 = -d, \omega + i0)\}. \quad (1)$$

The factor D depends on the mass density and permittivity of the medium, scattering geometry, and incident photon frequency and polarization. G_{33} is the (x_3, x_3) component of the Fourier (frequency and wave vector) domain surface elastodynamic Green's-function tensor $G_{ij}(x, t)$, evaluated at the outer surface $x_3 = -d$ of the film. A brief outline of the method of calculation of G_{33} appears below, and further details of the calculation are provided in the appendix.

In each of the substrate and layer for a given value of k_{\parallel} and ω , the equations of motion admit six plane wave solutions. These partial waves pertain to different wave-vector components $k_3^{(n)}$ perpendicular to the free surface, which may be real or complex and are the solutions of the sextic Christoffel characteristic equation. For the layer, all six

phase-matched plane waves ($n = 1, 2, \dots, 6$) are used; while for the substrate only the three outgoing plane waves ($n = 7, 8, 9$) are retained, as discussed by Farnell and Adler.⁷ The outgoing waves are either homogeneous with $k_3^{(n)}$ real and having ray vectors $\mathbf{v} = \partial\omega/\partial\mathbf{k}$ directed into the interior of the substrate, or evanescent waves with $\text{Im}(k_3^{(n)}) > 0$, so that their amplitudes fall off into the interior. The boundary conditions on the surface tractions and displacements provide nine equations for determining the partial wave amplitudes. The Green's function $G_{33}(k_{\parallel}, x_3 = -d, \omega)$ is obtained as the superposition of the six partial waves in the film:

$$G_{33}(k_{\parallel}, x_3 = -d, \omega) = \sum_{n=1}^6 \frac{i}{\omega} (B^{-1})_3^{(n)} U_3^{(n)} \exp\{-ik_3^{(n)} d\}, \quad (2)$$

where B is the boundary-condition matrix, and $U_3^{(n)}$ are the x_3 components of the polarization vectors for the six modes in the layer.

In surface Brillouin scattering, k_{\parallel} is determined by the experimental arrangement and scattering geometry, and $\text{Im}\{G_{33}(k_{\parallel}, x_3 = -d; \omega + i0)\}$ and hence the Brillouin scattering intensity $I(\omega)$ is a function of the angular-frequency shift in the measured spectrum. The Brillouin-scattering spectrum consists of one or more sharp lines associated with true Rayleigh or Sezawa surface waves and then at higher frequencies a continuum of excitations extending from a threshold, known as the transonic state, to higher frequencies. True surface waves are conditioned by the vanishing of $|B|$, which causes B^{-1} to become singular, and G to have a pole on the real axis for ω or v . The continuum, known as the Lamb shoulder, represents the contribution of bulk waves to surface Brillouin scattering. Under certain circumstances, the Brillouin spectrum displays one or more broadened peaks within the frequency region of the Lamb shoulder; these peaks or resonances are associated with pseudo-SAW's, which correspond to poles of G that lie off the real axis in the complex plane. For the type of pseudo-SAW that has been most often considered in the literature,⁷ the pole is not too far off the real axis and is well away from the transonic state. Under these conditions, the pseudo-SAW is in the nature of an attenuated SAW, with velocity determined by the real part of the pole and attenuation by the imaginary part. Along the real axis, $|B|$ displays a deep minimum and G_{33} displays a sharp, approximately Lorentzian maximum at the pseudo-SAW velocity. The pseudo-Sezawa wave we are considering in this paper is, however of a quite different nature, being located very close to the transonic state. Far from being Lorentzian in shape, the peak in G_{33} is asymmetric, having a sharp leading and gradual trailing edge. The Green's-function formalism is particularly convenient for describing the spectrum of this type of excitation. Knowledge of the position of the pole in the complex plane on the other hand, does not on its own reveal the shape of the peak in the spectrum, and moreover, $|B|$ does not possess a minimum along the real axis in the vicinity of the peak.

IV. RESULTS AND DISCUSSION

In Fig. 3, we present the measured anti-Stokes SBS spectra for the [100] direction referred to the (001) silicon sub-

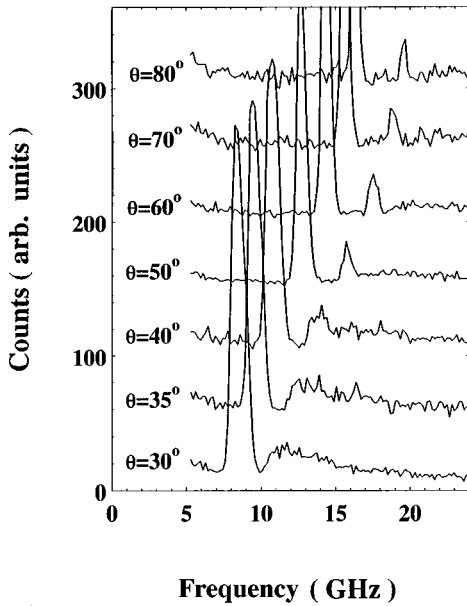


FIG. 3. Measured anti-Stokes Brillouin spectra at different scattering angles θ for the [100] direction referred to the (001) crystalline-silicon substrate for sample A.

strate for sample A at different scattering angles θ . In each case the intense central peak resulting mainly from elastic scattering has been removed for clarity. The dominant peak for each value of θ corresponds to the Rayleigh SAW. However, it is observed that an additional peak appears at larger frequency shifts within the region of the Lamb shoulder, but only when the scattering angle θ is larger than 40° . For samples B and C, similar peaks were measured; in particular for sample C, the feature is observed near the threshold of the Lamb shoulder as a broad asymmetric peak. In samples D and E, for which the thickness of the amorphous silicon layer is smaller, this additional feature was absent.

As discussed and justified in Sec. II, we base our explanation of the features present in the SBS spectra on a simple model: an elastically uniform isotropic amorphous silicon layer on the (001) silicon surface. Additional tests were carried out to confirm the assumed properties of the amorphous layer. In the first of these, we performed SBS measurements of the azimuthal angular dependence of the Rayleigh SAW velocity for sample A at a scattering angle θ of 70° . The results showed minimal anisotropy, in marked contrast to the fairly high anisotropy for the crystalline (001) silicon surface measured recently by Stoddart, Comins, and Every¹³ using SBS. In the second test, the value of the Rayleigh SAW velocity for amorphous silicon was determined as 4250 m/s, which is in agreement with that of earlier measurements on amorphous silicon,^{10,11} and considerably lower than the values in crystalline silicon. These results are consistent with the model of a layer completely amorphized by the high-fluence ion bombardment employed on the silicon surface. In the third test, Raman spectra at room temperature were measured for the samples and the results are shown in Fig. 4 for sample B and crystalline silicon. In the spectrum for sample B, the crystalline-silicon peak near 520 cm^{-1} is totally absent and instead there is a weak broad peak around 450 cm^{-1} , which is consistent with the observations reported in Ref. 10 for amorphous silicon formed by krypton ion bombardment.

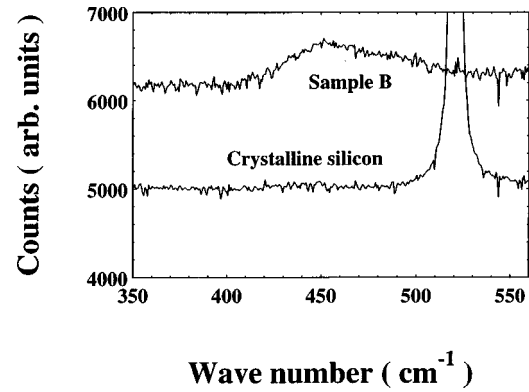


FIG. 4. Raman spectra for sample B and crystalline silicon. Spectra were measured at room temperature.

For each of the samples, the layer thickness is determined by the TRIM 92 simulation as described in Sec. II and Fig. 1; for samples A, B, and C these are 230, 190, and 150 nm, respectively.

The measured Brillouin spectra are well accounted for by theory when appropriate values of the parameters, elastic constants, and mass densities of amorphous and crystalline silicon and layer thickness are used in the calculation of the surface Green's function. For crystalline silicon we have used the literature values:⁷ mass density $\rho = 2.332\text{ g/cm}^3$, $C_{11} = 165.7$, $C_{12} = 63.9$, and $C_{44} = 79.6\text{ GPa}$, respectively. For the amorphous silicon layer, we used the reported value of the mass density of sputtered amorphous silicon, namely, 0.95 of that of crystalline silicon.¹¹ We note that this near equality in the respective densities of the crystalline and amorphous forms indicates that amorphous silicon produced by different methods is unlikely to exhibit significant differences in density. Accordingly, the behavior of the acoustic excitations will be dominated by the values of the elastic constants of the layer and the substrate.

In determining the elastic properties of the amorphous-silicon layer we use a combination of data, rather than relying solely on the least squares fitting to the SAW velocity dispersion. This latter procedure, while being successful in certain cases,^{22,23} has been found to lead to significant uncertainties in some of the elastic constants in others.²⁴ As will be described later in the paper, measurements were made of the values of the velocities corresponding to the minimum in the Lamb shoulder that occurs near the longitudinal-wave threshold. These velocities were used together with those determined from the Rayleigh peaks in a least-squares fitting procedure.²⁵ Minimization of

$$\chi^2 = \sum_R (V_{\text{cal}}^i - V_{\text{meas}}^i)^2 + \sum_L (V_{\text{cal}}^i - V_{\text{meas}}^i)^2 \quad (3)$$

with respect to variation of the values of the elastic constants of the layer was carried out, where V_{cal}^i are the velocities calculated from the surface Green's function, and V_{meas}^i are the measured velocities. In the summations, we use the complete set of data for the Rayleigh wave (the first term), while the data for the minimum in the Lamb shoulder (the second term) are restricted to the cases of sufficiently thick films (see the detailed discussion to follow). The best fit values of the elastic constants of the amorphous silicon layer are C_{11}

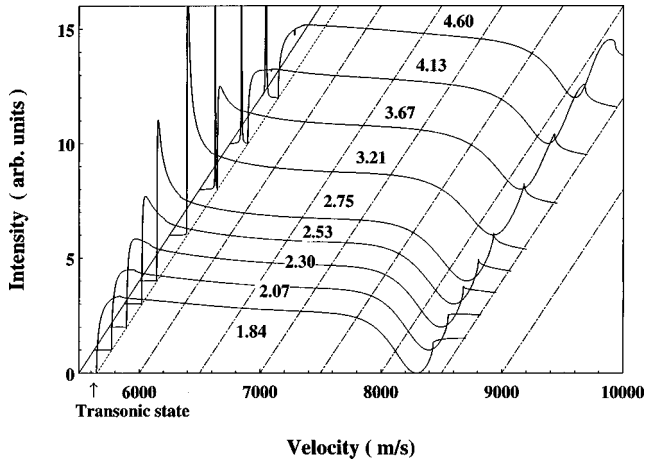


FIG. 5. Calculated Brillouin spectra for various of $k_{\parallel}d$. The dotted line marked with an arrow indicates the transverse threshold of the Lamb shoulder or the transonic state.

= 138 GPa and C_{44} = 48 GPa. These values are within 10% of the elastic constants of amorphous silicon (containing 15% hydrogen) measured by Brillouin scattering,¹¹ while the transverse and longitudinal-wave velocities of the layer are calculated to be 4620 and 7880 m/s, respectively, being within 5% of those for sputtered amorphous silicon measured by a crystal-resonator method.¹²

Having established the elastic constants of the amorphous-silicon layer, the SBS spectrum can be calculated using the Green's-function formalism discussed in Sec. III. In Fig. 5, a series of calculated SBS spectra are shown for the [100] direction referred to the (001) silicon surface. They are displayed as a function of wave velocity for ease of comparison with the slowness curves for the (010) plane in silicon shown in Fig. 6. For clarity, the Rayleigh SAW peak is not shown in Fig. 5.

The range of $k_{\parallel}d$ values from 1.84 to 4.6 used in Fig. 5 corresponds to the region in which the first-order Sezawa mode appears. For the smallest values of $k_{\parallel}d$, the SBS spectrum is close to that of crystalline silicon. In addition to the Rayleigh SAW, there is the considerably less dominant Lamb shoulder that begins at the transverse-wave threshold velocity (5648 m/s) and has a sharp minimum near the longitudinal threshold (8344 m/s). Close inspection reveals a small kink in the Lamb shoulder at the fast transverse (FT) threshold (5844 m/s). Referring to Fig. 6, the transverse threshold corresponds to the limiting point on the slow transverse (ST) slowness curve where $S_{\parallel} = k_{\parallel}/\omega$ is a maximum, and where the ray vector, which is perpendicular to the slowness surface, is parallel to the physical surface of the sample. At larger values of S_{\parallel} , corresponding to smaller velocities, all solutions for the slowness component $S_3 = k_3/\omega$ are complex and correspond to inhomogeneous waves; the maximum value of S_{\parallel} is thus known as the transonic state. For an isotropic solid, the slowness curves are circles, and the transonic state coincides with the transverse slowness along the surface, $S_T = (\rho/C_{44})^{1/2}$, but this is not generally true for anisotropic solids as Fig. 6 demonstrates. True SAW's such as Rayleigh and Sezawa waves occur in the subsonic range of velocities, while pseudo SAW's and the Lamb shoulder lie in the supersonic range.

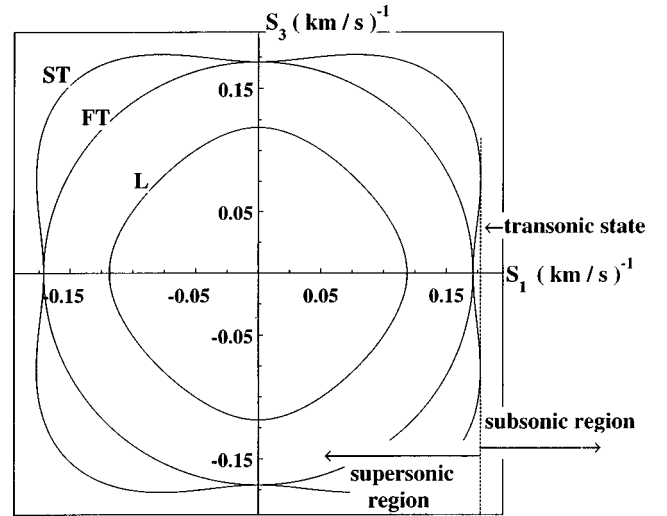


FIG. 6. The slowness curve of silicon for the (010) plane. The dashed line corresponds the transonic state. The solid curves correspond the slowness curves for longitudinal (L), FT and ST bulk waves.

In Fig. 5, we observe that as $k_{\parallel}d$ increases from the smallest value considered above, a broad asymmetric resonance peak, which can be identified as a pseudo-Sezawa wave appears in the Lamb shoulder near the transverse threshold. It becomes progressively sharper, moving ever closer to the transverse threshold of the Lamb shoulder, until at a critical value of $k_{\parallel}d$, a true surface wave, the Sezawa wave, separates from the Lamb shoulder and moves into the subsonic region. Initially the Sezawa wave has a very small integrated intensity, but with increasing $k_{\parallel}d$, it moves further from the Lamb shoulder and grows in intensity. Immediately after the Sezawa wave has separated, the asymmetric peak is still present within the Lamb shoulder and close to the threshold (see the spectrum for $k_{\parallel}d = 3.67$ in Fig. 5). However, as the Sezawa wave moves further from Lamb shoulder, the asymmetric peak becomes broad again with its phase velocity increasing, and subsides into the Lamb shoulder.

The essential difference between the Sezawa and pseudo-Sezawa waves is understood in term of k_3 values of the partial waves. For the Sezawa wave, which lies in subsonic range in Fig. 6, the partial waves in the substrate all have a complex value of k_3 , and the corresponding displacement amplitudes decrease in an exponential fashion into the interior of the substrate. These properties allow the Sezawa wave to propagate without attenuation along the surface and thus it is a true surface wave. In the case of the pseudo-Sezawa wave, which lies in the supersonic range in Fig. 6, one or more of the partial waves in the substrate has a real value of k_3 . This bulk-wave component carries energy away from the surface into the interior of the substrate and cause the wave to decay with distance. We use the term pseudo-Sezawa wave here because this particular pseudo SAW is so closely linked to the true Sezawa wave.

Fig. 7 shows the measured and calculated dispersion curves for the Rayleigh SAW and Sezawa-type modes. The dispersion curves of the Rayleigh and Sezawa-like modes (solid lines) are calculated using best fit elastic constants determined by comparison with our SBS measurements. There are also calculated curves for the higher order Sezawa

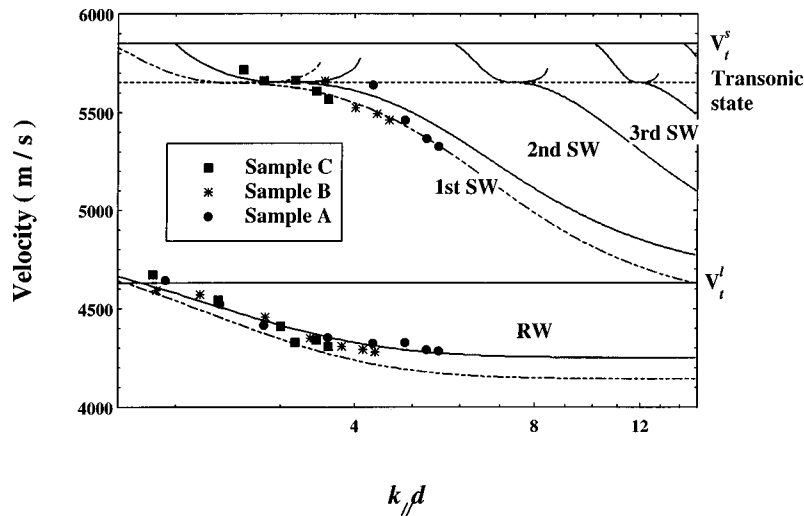


FIG. 7. Dispersion relations for the [100] direction. The two solid lines marked V_t^s and V_t^l represent the transverse bulk-wave velocity for the crystalline-silicon substrate and the amorphous silicon layer, respectively. The dotted-horizontal line indicates the transonic state. The solid curves represent calculated dispersion curves based on the model of a uniform amorphous layer on the (001) silicon surface and the elastic constants of the layer obtained from the present measurements. Dashed curves represent calculated dispersion curves from the elastic constants given in the literature (Ref. 11). RW, Rayleigh wave; 1st SW, etc., different orders of Sezawa waves.

waves, but these modes were not observed in the present experiments. For purpose of comparison, the dispersion curves of the Rayleigh-SAW and the first Sezawa-like excitation are also calculated using the literature values¹¹ of the elastic constants of amorphous silicon. The agreement is within 2%, which is reasonably good, bearing in mind the completely different methods employed in the production of the amorphous silicon and the likelihood of small physical differences. For large $k_{\parallel}d$, the Rayleigh SAW velocity tends asymptotically to a constant value (4250 m/s), which is the phase velocity of the Rayleigh wave on the surface of bulk amorphous silicon. This velocity is in good agreement with earlier measurements on amorphous silicon,^{10,11} and is much lower than that of crystalline silicon in the [100] direction in the (001) surface (~ 4917 m/s at $k_{\parallel}d=0$). The two horizontal lines labeled V_t^l and V_t^s are transverse bulk-wave-phase velocities in the layer and in the substrate, respectively. A lower transverse bulk-wave-phase velocity in the layer as compared with that of the substrate is necessary in order for Sezawa waves to exist. The horizontal-dashed line corresponds to the transonic state in the substrate. The curves below the transonic state are the various orders of Sezawa waves, while curves for the pseudo-Sezawa waves lie above the transonic state. Also shown in Fig. 7 are the phase velocities measured by SBS as a function of $k_{\parallel}d$ not only of the Rayleigh SAW for samples A, B, and C as discussed previously, but also for the additional peaks in the region of the Lamb shoulder, such as those illustrated in Fig. 3 for sample A. These measured data are in fairly good agreement (see the discussion below) with the calculated curves for the first-order Sezawa wave or pseudo-Sezawa wave, respectively. As expected and found for samples E and D, and in general for small values of $k_{\parallel}d$ in the samples A, B, and C, the Sezawa-type modes are absent.

Elastic constant values for amorphous silicon that produce a good fit for the dispersion of the measured Rayleigh-SAW velocities, result in a calculated Sezawa-wave dispersion curve in which the measured velocities are slightly lower

than the calculations. The discrepancy is small, being within 2% and can be explained qualitatively considering the effect of the tail to the amorphous region in which the silicon is partially amorphous. Here the elastic constants will lie between those of amorphous and crystalline silicon rather than having the larger crystalline values assumed in the theory. Since the Rayleigh SAW is localized mainly near the free surface of the layer, this tail region has little effect on this mode, so the velocity of the Rayleigh SAW will not be significantly affected by the presence of this tail. On the other hand, the Sezawa wave extends into the tail region and a small reduction of the phase velocity would therefore be expected. The nonuniformity of the elastic constants in the tail of the ion-implanted layers does have an effect on the phase velocity of the Rayleigh SAW when the layer thickness is sufficiently small, and this will be discussed elsewhere.

In Fig. 8, the anti-Stokes SBS spectra for the samples B (dashed curves) and C (solid curves) are shown for a range of scattering angles corresponding to $k_{\parallel}d$ values from 1.83 to 4.33. These spectra may be compared with the calculated spectra shown in Fig. 5, which cover approximately the same range of $k_{\parallel}d$ values. The measured spectra in the Lamb shoulder region are weak and have a relatively poor signal to noise ratio. Furthermore, due to the limitations of the interferometer, certain of the very sharp features predicted in the theoretical spectrum are incompletely resolved. Nonetheless, it is possible to observe most of the predicted features in the experimental spectra.

At the lowest values of $k_{\parallel}d$, e.g., near 1.8, both the theoretical and experimental spectra show the Lamb-shoulder region devoid of Sezawa-like peaks. With increase in $k_{\parallel}d$, in the range 2.3–3.2, the theoretical spectra predict the growth of the pseudo-Sezawa peak with a sharp leading edge at the lower velocity and a markedly asymmetric trailing edge. In experimental spectra this asymmetric shape of the peak is evident; this is seen readily in the spectra for $k_{\parallel}d=2.59$ and 2.81 in Fig. 8. It is noted that one is dealing purely with the pseudo-Sezawa wave for such low values of $k_{\parallel}d$. For suffi-

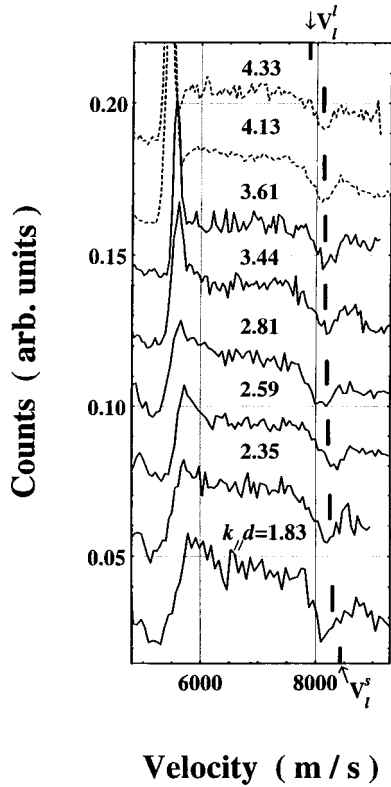


FIG. 8. Anti-Stokes Brillouin spectra for sample *B* (dashed curves) and *C* (solid curves). The spectra were measured for different $k_{\parallel}d$ for the [100] direction referred to the (001) crystalline-silicon substrate. The marks V_t^s and V_t^l show the phase velocity of the longitudinal threshold of the Lamb shoulder for crystalline silicon and for amorphous silicon, respectively. In each case the bars indicate the calculated positions of the minimum in the Lamb shoulder.

ciently large $k_{\parallel}d$, e.g., 3.67 in the theoretical spectra, the Sezawa wave has separated from the Lamb continuum and the peak is becoming more and more intense, while the pseudo-Sezawa component is much reduced in intensity. In the experimental spectra for the larger measured values of $k_{\parallel}d$, namely 3.44 and 3.61, the resolution of the interferometer is insufficient to fully separate the Sezawa wave peak from the Lamb shoulder. However, it is evident that the measured peak is considerably more symmetrical and obviously sharper, in contrast to the peaks in the spectra for $k_{\parallel}d = 2.59$ and 2.81. The continuum of excitations near the transverse threshold is substantially reduced, the intensity of the Sezawa peak has increased, and its velocity is reduced. Thus, the dominant contribution to the peak arises from the Sezawa wave, which is in satisfactory agreement with theory. For the values of $k_{\parallel}d$ above 4.13, the Sezawa mode is separated from the Lamb shoulder, and is becoming more intense. In the experimental spectra, we can see that the intense peak has started to separate from the Lamb shoulder.

In Fig. 5, the theoretical spectra show a sharp minimum in the Lamb shoulder near the longitudinal threshold. This minimum moves towards lower values of velocity as the scattering angle and hence k_{\parallel} (or $k_{\parallel}d$ for a particular sample) increases. For bulk materials, this minimum coincides with the longitudinal threshold, and its position can be directly calculated from the elastic constants. For isotropic materials

and some special directions, for example, the [100] direction in the (001) surface for the cubic system, its position is directly determined by the value of C_{11}/ρ . In our case of an elastically isotropic layer on the (001) silicon surface, for the [100] direction the position of the minimum is determined almost exclusively by the parameter $k_{\parallel}d$ and the respective values of C_{11} and ρ of the layer and substrate. Hence, the experimental observation of this minimum provides information on these parameters. Thanks to the high surface quality of the samples and high efficiency of the silicon avalanche photodiode detector, these subtle features can be observed experimentally as shown in Fig. 8. To the best of our knowledge, this is the first observation of the shift of the minimum in the Lamb shoulder with parameter $k_{\parallel}d$. The indicators V_t^s and V_t^l in Fig. 8 show the phase velocity of the respective longitudinal thresholds in the Lamb shoulder for crystalline silicon and amorphous silicon. In spite of the very low intensities of the signals in the Lamb shoulder region and the resulting noise in the experimental spectra, it is seen that, for values of $k_{\parallel}d$ above 2.81, a progressive variation can be observed in the minimum of the Lamb shoulder from a position at higher velocities to lower velocities as $k_{\parallel}d$ increases and it gradually approaches the value for amorphous silicon. For small values of $k_{\parallel}d$ below 2.81, there is a small discrepancy between the measured minima and the theoretical predictions. This is understandable, since for small values of $k_{\parallel}d$, the corresponding acoustic wavelength is large, and the effect of the tail to the amorphous region, in which the silicon is partly amorphous is no longer negligible. The bars in Fig. 8, show the calculated positions of the minimum using elastic constants obtained from the Rayleigh SAW velocity data together with the positions of the minimum for $k_{\parallel}d$ over 2.81.

V. CONCLUSION

A series of Brillouin spectra have been measured for amorphous-silicon layers formed by Ar-ion bombardment of (001) silicon surfaces. In addition to the Rayleigh SAW, an additional peak is present near the low-frequency threshold of the Lamb shoulder. This peak is only observed at large-scattering angles or for large-layer thickness. Calculations confirm that these peaks are due to Sezawa or pseudo-Sezawa waves, the latter lying within the Lamb shoulder. The threshold of the Lamb shoulder occurs at the transonic state, which for anisotropic crystalline silicon, lies below V_t^s . The pseudo-Sezawa waves are most pronounced in the velocity region from the transonic state to V_t^s , as an asymmetric peak in the calculated SBS spectra, and this is confirmed in some detail by the experimental observations.

We find both from experiment and calculations that a minimum in the Lamb shoulder near the longitudinal threshold can be modified by varying $k_{\parallel}d$. The experimental observation of this minimum as a function of layer thickness or scattering parameter k_{\parallel} is of value in investigating the elastic properties of the layer.

ACKNOWLEDGMENTS

We gratefully acknowledge the assistance of M. Naidoo of the Schonland Research Center for Nuclear Sciences in

the ion bombardment of the samples. Financial support of these studies was provided by the Foundation for Research and Development, Pretoria.

APPENDIX: CALCULATION OF THE SURFACE GREEN'S FUNCTION

There are a number of experimental groups worldwide presently engaged in Brillouin scattering studies and that are using the Green's-function approach in their calculations, and we have received a number of requests for our codings and for a simple explanation of the method for reference purposes. In response we set out in this appendix our method for calculating $G_{33}(k_{\parallel}, x_3, \omega)$, and thereby the Brillouin intensity.

In the case of an opaque layer, the scattering occurs at the free surface of the layer and requires the evaluation of $G_{33}(k_{\parallel}, x_3 = -d, \omega)$, while for a thin-transparent layer on an opaque solid the scattering occurs mainly at the interface and requires the evaluation of $G_{33}(k_{\parallel}, x_3 = 0, \omega)$. We are disregarding elasto-optic scattering and interference between this and ripple scattering at the two surfaces, which under certain circumstances can be quite pronounced. Our main concern here is with the surface dynamics, and by the means described below we can account accurately for peak positions but not always as well for their intensities where elasto-optic scattering and interference effects are important. $G_{33}(k_{\parallel}, x_3 = -d, \omega)$ is the (x_3, x_3) component of the Fourier-domain Green's tensor of the system for force and displacement response at the surface of the layer.

In evaluating the response, the boundary conditions are continuity of the stress components (traction forces) $\sigma_{l3}(k_{\parallel}, x_3 = 0, \omega)$ and displacement field \mathbf{u} at the interface, and

$$\sigma_{l3}(k_{\parallel}, x_3 = -d, \omega) = -\delta_{l3} \quad (\text{A1})$$

at the free surface. In evaluating $G_{33}(k_{\parallel}, x_3 = 0, \omega)$, the boundary conditions on the stress field become

$$\sigma_{l3}(k_{\parallel}, x_3 = 0_-, \omega) - \sigma_{l3}(k_{\parallel}, x_3 = 0_+, \omega) = -\delta_{l3} \quad (\text{A2})$$

for the interface and

$$\sigma_{l3}(k_{\parallel}, x_3 = -d, \omega) = 0 \quad (\text{A3})$$

for the free surface. In each of the two media, substrate, and layer, the displacement field is required to satisfy the equations of motion for an homogeneous elastic continuum

$$\rho \frac{\partial^2 u_i}{\partial t^2} = C_{ijkl} \frac{\partial^2 u_l}{\partial x_j \partial x_k}, \quad (\text{A4})$$

where C_{ijkl} is the elastic-modulus tensor, ρ is the mass density, and u_i are the particle displacement components in the individual media. For each value of k_{\parallel} and ω , Eq. (A4) admits six plane-wave solutions for which the third component $k_3^{(n)}$, $n = 1, \dots, 6$ of \mathbf{k} is obtained as a real or complex root of the sextic-characteristic equation

$$|C_{ijkl} k_j k_k - \delta_{il} \rho \omega^2| = 0, \quad (\text{A5a})$$

and the associated polarization vector U_i is obtained from

$$(C_{ijkl} k_j k_k - \delta_{il} \rho \omega^2) U_i = 0. \quad (\text{A5b})$$

For the layer, all six waves $k_3^{(n)}$, $n = 1, \dots, 6$ are used; while for the substrate only the three outgoing waves, which we enumerate $k_3^{(n)}$, $n = 7, 8, 9$ are retained, and the three incoming waves are discarded.⁷ The outgoing waves are either homogeneous, with $k_3^{(n)}$ real and with ray vectors $\mathbf{v} = \partial\omega/\partial\mathbf{k}$ directed into the interior of the substrate, or evanescent waves with $\text{Im}(k_3^{(n)}) > 0$, so that their amplitudes fall off into the interior.

The solution we are seeking that satisfies the boundary conditions, in the layer takes the form of a superposition of the six plane waves ($n = 1, 2, \dots, 6$):

$$u_i^-(k_{\parallel}, x_3, \omega) = \sum_{n=1}^6 A_3^{(n)} U_i^{(n)} \exp\{ik_3^{(n)} x_3\}, \quad (\text{A6})$$

and in the half space of the three outgoing plane waves ($n = 7, 8, 9$):

$$u_i^+(k_{\parallel}, x_3, \omega) = \sum_{n=7}^9 A_3^{(n)} U_i^{(n)} \exp\{ik_3^{(n)} x_3\}. \quad (\text{A7})$$

From the stress-strain relationship, $\sigma_{lm} = C_{lmnp} \partial u_p / \partial x_q$ for the layer and Eq. (A6) it follows that the surface tractions are given by

$$\sigma_{l3}(k_{\parallel}, x_3 = -d, \omega) = i\omega \sum_{n=1}^6 A_3^{(n)} B_l^{(n)}, \quad (\text{A8})$$

where

$$B_l^{(n)} = \sum_{pq} C_{3lpq}^- U_p^{(n)} k_q^{(n)} \exp\{-ik_3^{(n)} d\} / \omega, \quad n = 1, 2, \dots, 6, \quad l = 1, 2, 3. \quad (\text{A9})$$

Comparing Eqs. (A1) and (A8), we obtain a set of three linear equations for the partial wave amplitudes $A_3^{(n)}$, namely,

$$\sum_{n=1}^6 B_l^{(n)} A_3^{(n)} = \begin{cases} \frac{i}{\omega} \delta_{3l}, & l = 1, 2, 3 \\ 0, & \end{cases} \quad (\text{A10})$$

for the surface and interface Green's functions, respectively.

Another three equations for the partial wave amplitudes arise from the stress conditions at the interface, which yield

$$\sum_{n=1}^9 B_l^{(n)} A_3^{(n)} = \begin{cases} 0 \\ \frac{i}{\omega} \delta_{3l}, & l = 4, 5, 6 \end{cases} \quad (\text{A11})$$

for the surface and interface Green's functions, respectively, where

$$B_l^{(n)} = \sum_{pq} C_{3(l-3)pq}^+ U_p^{(n)} k_q^{(n)} / \omega, \quad n = 7, 8, 9, \quad l = 4, 5, 6 \quad (\text{A12})$$

and

$$B_l^{(n)} = - \sum_{pq} C_{3(l-3)pq}^- U_p^{(n)} k_q^{(n)} / \omega, \\ n = 1, 2, \dots, 6, \quad l = 4, 5, 6. \quad (\text{A13})$$

Finally, there are three equations for the partial wave amplitudes arising from continuity of the displacement field at the interface, which yield

$$\sum_{n=1}^9 B_l^{(n)} A_j^{(n)} = 0, \quad l = 7, 8, 9, \quad (\text{A14})$$

where

$$B_l^{(n)} = U_{l-6}^{(n)}, \quad l = 7, 8, 9, \quad n = 7, 8, 9, \quad (\text{A15})$$

and

$$B_l^{(n)} = -U_{l-6}^{(n)}, \quad l = 7, 8, 9, \quad n = 1, 2, \dots, 6. \quad (\text{A16})$$

The solution of the nine equations for $A_3^{(n)}$ above takes the form

$$A_3^{(n)} = \frac{i}{\omega} (B^{-1})_3^{(n)}. \quad (\text{A17})$$

By substituting these results for $A_3^{(n)}$ into Eq. (A6), we obtain the displacement Green's function for the free surface of the layer,

$$G_{33}(k_{\parallel}, x_3 = -d, \omega) = \sum_{n=1}^6 \frac{i}{\omega} (B^{-1})_3^{(n)} U_3^{(n)} \exp\{-ik_3^{(n)}d\}, \quad (\text{A18})$$

and for the interface

$$G_{33}(k_{\parallel}, x_3 = 0, \omega) = \sum_{n=1}^6 \frac{i}{\omega} (B^{-1})_3^{(n)} U_3^{(n)}. \quad (\text{A19})$$

-
- ¹P. Mutti, C. E. Bottani, G. Ghislotti, M. Beghi, G. A. D. Briggs, and J. R. Sandercock, in *Advances in Acoustic Microscopy*, edited by A. Briggs (Plenum, New York, 1995), Vol. 1, p. 249.
- ²V. Bortolani, F. Nizzoli, G. Santoro, A. Marvin, and J. R. Sandercock, *Phys. Rev. Lett.* **43**, 224 (1979).
- ³V. Bortolani, F. Nizzoli, G. Santoro, and J. R. Sandercock, *Phys. Rev. B* **25**, 3442 (1982).
- ⁴J. M. Karanikas, R. Sooryaakumarand, and J. M. Phillips, *Phys. Rev. B* **39**, 1388 (1989).
- ⁵G. Ghislotti, C. E. Bottani, and P. Mutti, *Phys. Rev. B* **51**, 9875 (1995).
- ⁶G. Ghislotti and C. E. Bottani, *Phys. Rev. B* **50**, 12 131 (1994).
- ⁷G. W. Farnell and E. L. Adler, in *Physical Acoustics*, edited by W. P. Mason and R. W. Thurston (Academic, New York, 1972), Vol. 9, p. 35; G. W. Farnell, in *Physical Acoustics*, edited by W. P. Mason and R. W. Thurston (Academic, New York, 1970), Vol. 6, p. 109.
- ⁸A. G. Every, W. Pang, J. D. Comins, and P. R. Stoddart, *Ultrasonics* **36**, 223 (1998).
- ⁹R. C. Birtcher, M. H. Grimsditch, and L. E. McNeil, *Phys. Rev. B* **50**, 8990 (1994).
- ¹⁰B. Bhadra, J. Pearson, P. Okamoto, L. Rehn, and M. Grimsditch, *Phys. Rev. B* **38**, 12 656 (1988).
- ¹¹W. Senn, G. Winterling, and M. Grimsditch, in *The Physics of Semiconductors 1978*, edited by B. H. Wilson (The Institute of Physics, London, 1978), p. 709.
- ¹²L. R. Testardi and J. J. Hauser, *Solid State Commun.* **21**, 1039 (1977).
- ¹³P. R. Stoddart, J. D. Comins, and A. G. Every, *Phys. Rev. B* **51**, 17 574 (1995).
- ¹⁴J. F. Ziegler, J. P. Biersack, and U. Littmark, *The Stopping and Range of Ions in Solids* (Pergamon, New York, 1985).
- ¹⁵A. H. Al-Bayati, K. G. Orrman-Rossiter, and D. G. Armour, *Surf. Sci.* **249**, 293 (1991).
- ¹⁶L. J. Huang, W. M. Lau, H. T. Tang, W. N. Lennard, I. V. Mitchell, P. J. Schultz, and M. Kasrai, *Phys. Rev. B* **50**, 18 453 (1994).
- ¹⁷P. R. Stoddart, J. Crowhurst, A. G. Every, and J. D. Comins, *J. Opt. Soc. Am. B* **15**, 2481 (1998).
- ¹⁸R. Loudon and J. R. Sandercock, *J. Phys. C* **13**, 2609 (1980).
- ¹⁹K. R. Subbaswamy and A. A. Maradudin, *Phys. Rev. B* **18**, 4181 (1978).
- ²⁰R. Loudon, *J. Phys. C* **11**, 2623 (1978).
- ²¹A. Marvin, V. Bortolani, F. Nizzoli, and G. Santoro, *J. Phys. C* **13**, 1607 (1980).
- ²²P. Mutti, Z. Sklar, G. A. D. Briggs, and C. Jeynes, *J. Appl. Phys.* **77**, 2388 (1995).
- ²³M. G. Beghi, C. E. Bottani, P. M. Ossi, T. A. Lafford, and B. K. Tanner, *J. Appl. Phys.* **81**, 672 (1997).
- ²⁴F. Nizzoli, R. Bhadra, O. F. de Lima, M. B. Brodsky, and M. Grimsditch, *Phys. Rev. B* **37**, 1007 (1988).
- ²⁵A. G. Every, *Phys. Rev. B* **22**, 1746 (1980).